

Topological insulators and superconductors based on p -wave magnets, electrical control and detection of a domain wall

Motohiko Ezawa¹

¹*Department of Applied Physics, The University of Tokyo, 7-3-1 Hongo, Tokyo 113-8656, Japan*
(Dated: August 20, 2024)

Altermagnets are time-reversal broken antiferromagnets, where the z component of the Néel vector is detectable by anomalous Hall effects. On the other hand, recently proposed p -wave magnets are time-reversal preserved antiferromagnets, and it is a highly nontrivial problem how to detect and control a domain wall. We study a one-dimensional hybrid system made of a p -wave magnet and a metal possessing the orbital degree of freedom. The hybrid system is a topological insulator without the spin-orbit interaction. There emerge two edge states per one edge, because the system is mapped to a set of two copies of a topological insulator. Each copy resembles the long-range Su-Schrieffer-Heeger model but it is topologically different. Topological interface states emerge at a domain wall in the p -wave magnet, which are charged due to the Jackiw-Rebbi mechanism. Consequently, a domain wall in the p -wave magnet will be controllable and detectable purely by electrical means. We also study Majorana fermions induced by proximity coupling of s -wave superconductivity and p -wave magnet.

I. INTRODUCTION

Magnetic domain walls are used for magnetic memories. For example, the magnetic race-track memory stores information by positions of domain walls[1, 2]. Readout and control of the position of a domain wall are essential. In ferromagnetic domain wall, it can be read out by observing magnetization. In addition, the position of a domain wall is shifted by applying a current due to the spin-transfer torque[3, 4]. On the other hand, it is difficult to read out and control the position of a domain wall in antiferromagnetic systems[5–11].

Altermagnets are the third type of magnets from the viewpoint of symmetry[12–14]. They are expected to be key players of next generation memories because they have both merits of ferromagnets and antiferromagnets. Although they are essentially antiferromagnets, the z -component of the Néel vector is detectable by measuring anomalous Hall conductance[15–18] because time-reversal symmetry is broken. The even-parity altermagnets including the d -wave, f -wave and i -wave altermagnets are main targets[15–27]. The band structure has momentum dependence in altermagnets[12–14, 24, 28, 29], which resembles d -wave, f -wave and i -wave superconductivity. There are some works[30–35] on the topological property of the d -wave altermagnet.

Recently, p -wave magnets were proposed[36], where the band structure has p -wave momentum dependence. They have odd parity and preserve time-reversal symmetry. It is pointed out that CeNiAsO is a p -wave magnet[36]. They are essentially antiferromagnets just as altermagnets are. Due to time-reversal symmetry, anomalous Hall effects are absent. It is a highly nontrivial problem to detect and control the magnetic domain wall in the p -wave magnet. The purpose of this work is to overcome this problem by exploring the topological property based on the p -wave magnet, which is yet to be done. The study of p -wave magnets is just a beginning stage[37].

In this paper, we study a hybrid system made of the p -wave magnet and one-dimensional metal possessing the orbital degree of freedom. We find the emergence of two-fold zero-energy topological edge states at each edge. It is under-

stood by making a unitary transformation, where the system becomes a set of two copies of one-dimensional topological insulator model. This model resembles the long-range Su-Schrieffer-Heeger (SSH) model but its topological properties are different although both models belong to the same topological class BDI. Next, we show that the Jackiw-Rebbi interface states emerge at the domain wall in the p -wave magnet. Because they are charged, the domain-wall position will be detectable and controllable electrically. We also study Majorana edge or interface states induced by the proximity coupling of s -wave superconductivity to a p -wave magnet.

II. p -WAVE TOPOLOGICAL CHAIN

A. Model

The p -wave magnet preserves time-reversal symmetry,

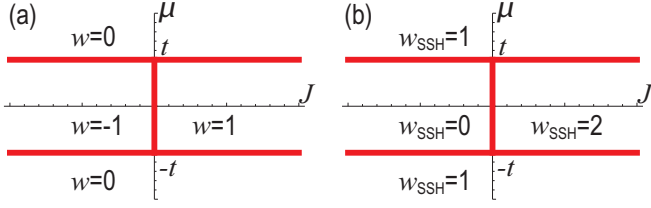
$$\Theta H_{\uparrow}(k) \Theta^{-1} = H_{\downarrow}(-k), \quad (1)$$

where $\Theta = i\sigma_y K$ is the generator of time-reversal symmetry with K taking complex conjugate. In the p -wave magnet, its effect on electrons is simply given in the form $\sigma_z \sin k$, which satisfies time-reversal symmetry[36].

We analyze the system where a one-dimensional metal with the orbital degree of freedom is attached to a p -wave magnet. The Hamiltonian is given by

$$H = \Gamma_{0z} \sum_x \frac{t}{2} \left(\hat{c}_x^{\dagger} \hat{c}_{x+1} + \hat{c}_{x+1}^{\dagger} \hat{c}_x \right) - \mu \hat{c}_x^{\dagger} \hat{c}_x \\ + \Gamma_{zx} \frac{J}{2i} \sum_x \left(\hat{c}_x^{\dagger} \hat{c}_{x+1} - \hat{c}_{x+1}^{\dagger} \hat{c}_x \right), \quad (2)$$

where \hat{c}_x (\hat{c}_x^{\dagger}) is annihilation (creation) operator of a fermion at the site x , $\Gamma_{\mu\nu} \equiv \sigma_{\mu} \otimes \tau_{\nu}$ is the gamma matrix with σ_{μ} the Pauli matrix for spins and τ_{ν} the Pauli matrix for orbitals; t is the hopping amplitude and μ is the chemical potential for the metallic wire, while J is the magnetization of the p -wave magnet. The meaning of the p -wave magnet is clarified in



the momentum-space representation. We note that there is no spin-orbit interaction in the Hamiltonian. The orbital degrees of freedom and their coupling to magnetization are the same as the Bernevig-Hughes-Zhang model[38]. They are studied also in d -wave altermagnets[32–34]. The Hamiltonian (2) is explicitly rewritten as

$$H = \sum_{x,\sigma,\tau} \frac{t}{2} \sigma \left(\hat{c}_{x,\sigma,\tau}^\dagger \hat{c}_{x+1,\sigma,\tau} + \hat{c}_{x+1,\sigma,\tau}^\dagger \hat{c}_{x,\sigma,\tau} \right) - \mu \hat{c}_{x,\sigma,\tau}^\dagger \hat{c}_{x,\sigma,\tau} + \frac{J}{2i} \sum_{x,\sigma,\tau} \tau \left(\hat{c}_{x,\sigma,\tau}^\dagger \hat{c}_{x+1,-\sigma,-\tau} - \hat{c}_{x+1,-\sigma,-\tau}^\dagger \hat{c}_{x,\sigma,\tau} \right) \quad (3)$$

where $\hat{c}_{x,\sigma,\tau}$ is an annihilation operator of a fermion with the spin σ and the orbital τ , $\sigma = \pm 1$ represents the spin degrees of freedom and $\tau = \pm 1$ represents the orbital degrees of freedom.

The Hamiltonian density reads in the momentum space as

$$H(k) = (t \cos k - \mu) \Gamma_{0z} + (J \sin k) \Gamma_{zx}, \quad (4)$$

where k is the momentum along the x -direction, $0 \leq k < 2\pi$. The $\sin k$ dependence is that of the p -wave magnet, which resembles the p -wave superconductor. Similar models are studied in literature[36]. The energy spectrum is given by

$$E(k) = \pm \sqrt{(t \cos k - \mu)^2 + (J \sin k)^2}, \quad (5)$$

where the energy is two-fold degenerated. The gap closing conditions are given by $|\mu/t| = 1$ and $J = 0$ with $|\mu/t| < 1$, which are illustrated by red lines in the J - μ plane in Fig.1(a).

B. Symmetry

The system has chiral symmetry, $\{H, \Gamma\} = 0$ with the chiral operator $\Gamma \equiv [\Gamma_{0z}, \Gamma_{zx}]/2i$. It has also time-reversal symmetry, $\Theta H(k) \Theta^{-1} = H(-k)$ with $\Theta = i\sigma_y$. In addition, there is particle-hole symmetry, $\Xi H(k) \Xi^{-1} = -H(-k)$ with $\Xi = \tau_x$. Then, the system belongs to the class BDI[39], whose topology is characterized by the class Z .

Chiral symmetry or particle-hole symmetry protects the existence of the edge states exactly at the zero energy. If we

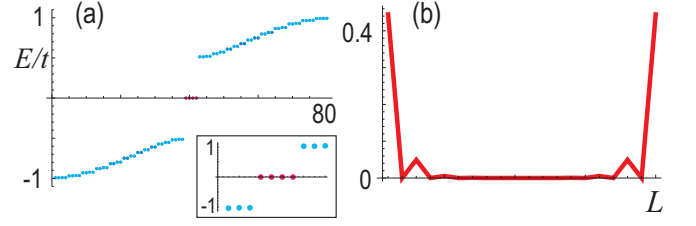


FIG. 2. (a) Energy spectrum for a finite chain described by Eq.(2). The inset shows an enlarged figure in the vicinity of the zero-energy, where four zero-energy edge states exist. The horizontal axis is the site index. Color palette for (a) indicates $|\psi_1|^2 + |\psi_L|^2$, which is given in Fig.5(d). (b) Spatial profile of the zero-energy states. We have set $J = 0.5t$, $\mu = 0$ and $L = 20$.

add a symmetry breaking perturbation term, the edge states may acquire nonzero energy but the spatial profile of the edge states persists in the first-order perturbation theory.

C. Topological edge states

We study a chain with a finite length. The energy spectrum is shown in Fig.2(a). There emerge four zero-energy edge states as in the inset of Fig.2(a). They are edge states as in Fig.2(b), where two zero-energy edge states are present at each edge. We show that they are topological edge states in the following subsection.

We show the energy spectrum as a function of J by setting $\mu = 0$ in Fig.3(a). The system is gapped for $J \neq 0$, where topological edge states emerge at the zero energy. There is a tiny gap around $J = 0$ in Fig.3(a), which is due to the finite-length effect owing to the overlap between two topological edge states. We show the energy spectrum as a function of μ in Fig.3(b), where the topological edge states are found for $|\mu/t| < 1$.

D. Winding number

We make a unitary transformation of $H(k)$ by a matrix U given by

$$U \equiv \begin{pmatrix} 1 & -i & 0 & 0 \\ 1 & i & 0 & 0 \\ 0 & 0 & 1 & i \\ 0 & 0 & 1 & -i \end{pmatrix}.$$

It follows that

$$U H U^{-1} = \tau_0 \otimes H_0, \quad (6)$$

with

$$H_0 \equiv \begin{pmatrix} 0 & q(k) \\ q^*(k) & 0 \end{pmatrix}, \quad (7)$$

and

$$q(k) \equiv t \cos k - \mu - iJ \sin k, \quad (8)$$

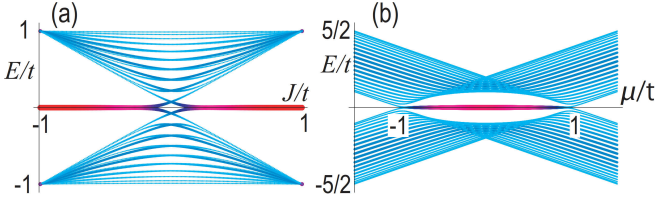


FIG. 3. (a) Energy spectrum as a function of J/t , where we have set $\mu = 0$. (b) Energy spectrum as a function of μ/t , where we have set $J = 0.5t$. Red curves indicate the topological edge states, while cyan curves indicate the bulk states. We have set $L = 20$. Color palette for (a) indicates $|\psi_1|^2 + |\psi_L|^2$, which is given in Fig.5(d).

where we have used the relations $U\Gamma_{0z}U^{-1} = \Gamma_{0x}$ and $U\Gamma_{zx}U^{-1} = \Gamma_{0y}$. The Hamiltonian is reduced to a set of two copies of the two-band model H_0 .

There is a hidden $SU(2)$ symmetry with respect to the first component in the Hamiltonian (6),

$$U_{SU(2)}^{-1}\tau_0U_{SU(2)} = \tau_0, \quad (9)$$

which protects the condition that the Hamiltonian (4) is decomposed into two copies of the Hamiltonian H_0 as in Eq.(6).

The topological number is the winding number defined by

$$w \equiv \frac{i}{2\pi} \int_0^{2\pi} q^{-1}(k) \frac{dq(k)}{dk} dk. \quad (10)$$

The winding number is $w = 1$ if $q(k)$ encircles the origin anticlockwisely in the complex plane made of $\text{Re}[q(k)]$ and $\text{Im}[q(k)]$, while it is $w = -1$ if $q(k)$ encircles the origin clockwise. On the other hand, it is $w = 0$ if $q(k)$ does not encircle the origin. We show the topological phase diagram in the J - μ plane in Fig.1(a). If $|\mu/t| < 1$, the winding number is $w = 1$ for $J > 0$ and $w = -1$ for $J < 0$. On the other hand, $w = 0$ for $|\mu/t| > 1$. It agrees with the number of topological edge states at one edge in the system H_0 .

E. Comparison to the SSH model

The Hamiltonian H_0 is mapped to the long-range SSH model H_{SSH} with $q_{SSH}(k) = t_A + t_B e^{-2ik} - \mu e^{-ik}$ by making a unitary transformation,

$$H_{SSH} = U_{SSH} H_0 U_{SSH}^{-1} \equiv \begin{pmatrix} 0 & q_{SSH}(k) \\ q_{SSH}^*(k) & 0 \end{pmatrix}, \quad (11)$$

where

$$U_{SSH} \equiv \begin{pmatrix} 1 & 0 \\ 0 & e^{ik} \end{pmatrix}, \quad q_{SSH}(k) = q(k) e^{-ik}, \quad (12)$$

and $t_A = (t - J)/2$, $t_B = (t + J)/2$. However, their topological properties are different, as shown in Figs.1(a) and (b). The difference is understood because the momentum-dependent unitary transformation U_{SSH} is nonlocal.

Indeed, the winding number is transformed as

$$\begin{aligned} w_{SSH} &\equiv \frac{i}{2\pi} \int q_{SSH}^{-1}(k) \frac{dq_{SSH}(k)}{dk} dk \\ &= \frac{i}{2\pi} \int \left(q^{-1}(k) \frac{dq(k)}{dk} - ik \right) dk = w + 1. \end{aligned} \quad (13)$$

It well explains the relation between these two models as in Fig.1(b).

III. JACKIW-REBBI ZERO-ENERGY INTERFACE STATE

We consider a domain wall configuration $J(x)$ in the p -wave magnet with length L . We assume that it has the same form as in the conventional magnet,

$$J(x) = J\sigma_z \tanh \frac{x - L/2 - 1/2}{\xi}, \quad (14)$$

satisfying $\lim_{x \rightarrow \infty} J(x) = J$ and $\lim_{x \rightarrow -\infty} J(x) = -J$, where the magnetization is flipped without in-plane components. The in-plane component is neglected, which is a good approximation for a very sharp domain wall, $\xi/L \ll 1$. We will discuss the effect of the in-plane canting later in the cases of the Bloch and Néel domain walls.

The gap closes at $k = \pm\pi/2$, $\mu = 0$ and $J = 0$. In its vicinity, the Hamiltonian H_0 is expanded as

$$H_0 = \begin{pmatrix} 0 & \mp tk' - \mu - iJ \\ \mp tk' - \mu + iJ & 0 \end{pmatrix}, \quad (15)$$

where we have defined $k' = k \mp \pi/2$. The Jackiw-Rebbi equations read[40]

$$\{\mp it\partial_x - \mu - iJ(x)\}\psi_B(x) = 0, \quad (16)$$

$$\{\mp it\partial_x - \mu + iJ(x)\}\psi_A(x) = 0, \quad (17)$$

where (ψ_A, ψ_B) is the basis vector of the Hamiltonian H_0 in the coordinate space.

Case (i): The solution is

$$\psi_A(x) = 0, \quad (18)$$

$$\psi_B(x) = \exp \left[\mp \frac{1}{t} \int^x (-J(x') + i\mu) dx' \right], \quad (19)$$

for $J > 0$ with $k' = k - \pi/2$, and for $J < 0$ with $k' = k + \pi/2$.

Case (ii): The solution is

$$\psi_A(x) = \exp \left[\mp \frac{1}{t} \int^x (J(x') + i\mu) dx' \right], \quad (20)$$

$$\psi_B(x) = 0, \quad (21)$$

for $J < 0$ with $k' = k - \pi/2$, and for $J > 0$ with $k' = k + \pi/2$.

In the case (i), with the use of Eq.(14), we obtain

$$\psi_B(x) = \sqrt{\frac{\Gamma(1/2 + |J|\xi/t)}{\sqrt{\pi}\xi\Gamma(|J|\xi/t)}} e^{i\mu x/t} \cosh^{-\frac{|J|\xi}{t}} \frac{x - \frac{L+1}{2}}{\xi}. \quad (22)$$

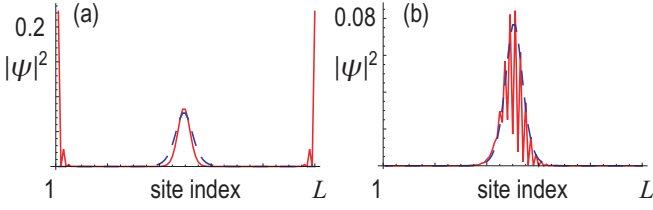


FIG. 4. (a) Spatial profile of the topological interface and edge states based on the Jackiw-Rebbi model. (b) Spatial profile of the topological interface states based on the magnetic domain-wall model. Red curves indicate numerical results based on the tight-binding model, while blue dashed curves indicate analytic solutions based on the Jackiw-Rebbi model. We have set $\xi = 5$ and $J = 0.5t$. We have used a chain with the length $L = 100$.

In the case (ii), we obtain Eq.(22) for $\psi_A(x)$. We show the spatial profile $|\psi(x)|^2 \equiv |\psi_A(x)|^2 + |\psi_B(x)|^2$ by a blue curve in Fig.4(a).

We also show the spatial profile $|\psi(x)|^2$ obtained numerically based on the tight-binding model by a red curve in Fig.4(a). The tight-binding result consists of the topological interface state at $x = L/2$ and the topological edge states at $x = 1, L$. There are four-fold degenerate topological interface states from $k = \pm\pi/2$ and from the two copies of the Hamiltonian H_0 .

One interface state has a half charge

$$\rho(x) = \frac{e}{2} |\psi(x)|^2, \quad (23)$$

according to the standard argument of the Jackiw-Rebbi state[40]. The charge is localized at the domain wall.

A. Bloch and Néel magnetic domain walls

The domain wall is actually canted and forms the Bloch or the Néel domain wall instead of the Jackiw-Rebbi type domain wall. The magnetization is

$$J(\sigma_z \cos \theta(x) + \sigma_x \sin \theta(x)) \quad (24)$$

for the Néel domain wall, and

$$J(\sigma_z \cos \theta(x) + \sigma_y \sin \theta(x)) \quad (25)$$

for the Bloch domain wall, where we have set

$$\cos \theta(x) = \tanh \frac{x-1/2}{\xi}, \quad \sin \theta(x) = \text{sech} \frac{x-1/2}{\xi}. \quad (26)$$

The energy spectrum is identical between the Bloch and Néel domain walls as shown in Fig.5(a). It is understood that these two systems are connected via unitary transformation,

$$H_{\text{Bloch}} = U^{-1} H_{\text{Néel}} U, \quad (27)$$

where

$$U \equiv \exp \left[\frac{i\pi}{4} \sigma_z \right] \quad (28)$$

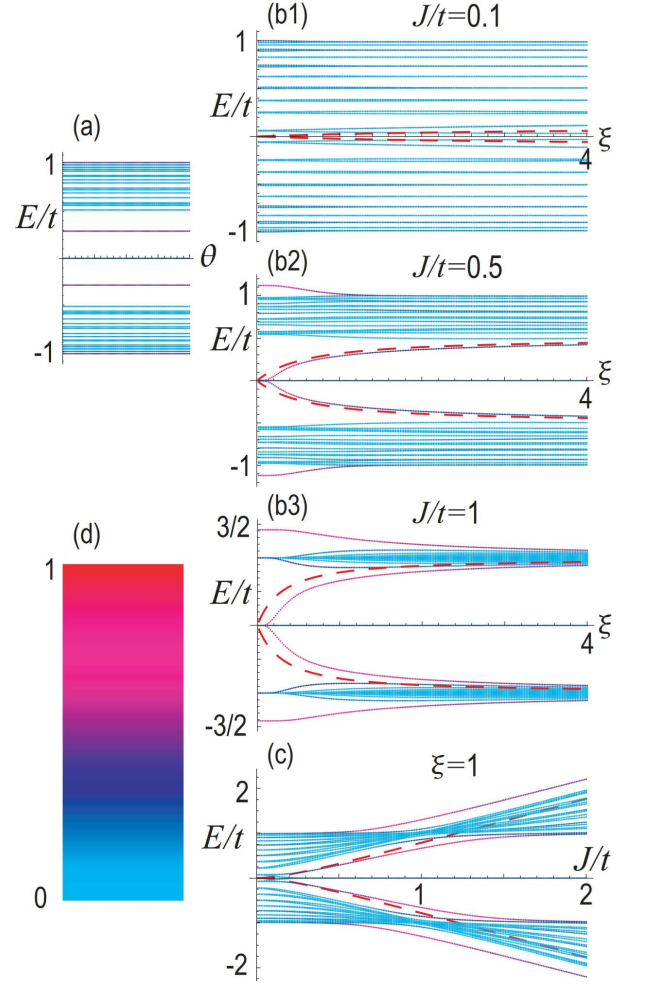


FIG. 5. (a) Energy spectrum as a function of θ . We have set $J = 0.5t$, $\xi = 1$ and $\mu = 0$. (b1), (b2) and (b3) Energy spectrum as a function of ξ . The red dashed curves indicate analytic solutions (29) based on the first-order perturbation theory. We have set (b1) $J = 0.1t$, (b2) $J = 0.5t$ and (b3) $J = t$ (c) Energy spectrum as a function of J/t . We have set $\mu = 0$. Red curves indicate the interface states, while cyan curves indicate the bulk or edge states. The length is $L = 20$. (d) Color palette indicates $|\psi_1|^2 + |\psi_L|^2$.

is the rotation along the z axis.

We estimate the energy of the Bloch and Néel domain walls. We use the first-order perturbation theory[41] in the presence of the term proportional to $\sin \theta(x)$ in Eqs.(24) and (25), where the eigenfunctions do not change but the energy is shifted. The first-order energy displacement is calculated with the use of Eq.(22) as

$$E = \int |\psi(x)|^2 \sin \theta(x) dx = J \frac{\Gamma^2 \left(\frac{1}{2} + \frac{J\xi}{t} \right)}{\Gamma \left(1 + \frac{J\xi}{t} \right) \Gamma \left(\frac{J\xi}{t} \right)}, \quad (29)$$

which is independent of the canted direction between the Bloch and the Néel domain walls.

We show the energy (29) as a function of ξ by dotted red curves in Fig.5(b1), (b2) and (b3). They will agree with the

numerical results on the energy spectrum in Fig.5(b1), (b2) and (b3), where the first-order perturbation theory and the continuum theory are not assumed. There is a tiny discrepancy at small ξ between the analytical and the numerical results. The numerical result shows a flat dispersion for $|J\xi/t| \ll 1$, while it is linear in the analytic result. It is due to the break down of the continuum approximation. For small ξ , Eq.(29) yields

$$E = J\pi\xi/t + o\left((J\pi\xi/t)^2\right). \quad (30)$$

On the other hand, for large ξ , Eq.(29) yields

$$E/J = 1 - t/4J\xi + (t/4J\xi)^2/2 + o\left((t/4J\xi)^3\right). \quad (31)$$

We show the energy spectrum as a function of J/t in Fig.5(c). It shows that the perturbation theory is valid for $J/t < 1$. J/t is much smaller than 1 in actual materials, which ensures the perturbation theory.

The interface states persist for the Bloch and the Néel domain walls but acquire nonzero energy as shown in Fig.4(b), whose spatial profile is well coincident with that of the Jackiw-Rebbi solution as depicted by a blue curve. It is understood as follows. The contribution of the in-plane component is tiny for a sharp domain wall. In this regime, we can treat the in-plane Hamiltonian as a perturbation term. Hence, the eigenstates remains as they are but the energy is modified in the first-order perturbation theory.

A comment is in order. The domain wall width is controlled by introducing the easy-axis anisotropy term $-AS_z^2$ to the system, which favors the spin pointing up or down. The domain wall width becomes smaller for larger easy-axis anisotropy.

IV. 2D MODEL

An actual sample has a finite width W . We consider a two-dimensional generalization of the model, where the Hamiltonian is given by

$$H_2 = (t \cos k_x + t \cos k_y - \mu) \Gamma_{0z} + (J \sin k_x) \Gamma_{zx}. \quad (32)$$

It is constructed from the one-dimensional model (4) with the replacement of the chemical potential μ by $\mu(k_y) = \mu - t \cos k_y$. The topological class of the class BDI in the two dimensions is trivial[39]. Nevertheless, there emerge topological edge states in the ladder geometry with finite width W as illustrated in Fig.6(a1), (b1) and (c1). Note that the ladder system with finite width is a one-dimensional system and belongs to the class Z .

We study a nanoribbon geometry based on the Hamiltonian (32). We find that there emerge 4 zero-energy topological edge states for odd width nanoribbons. Examples for the width $W = 2, 3, 4$ are shown in Fig.6(a2), (b2) and (c2).

This even-odd effect with respect to W is understood as follows. The Hamiltonian is actually made of two copies as in Eq.(6). In the vicinity of the zero energy, each Hamiltonian is well approximated by two chains with length W at $x = 1$ and

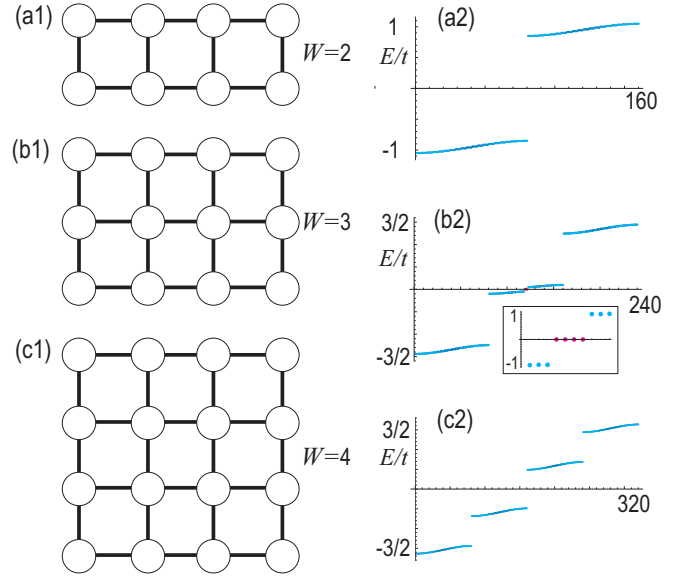


FIG. 6. Illustration of (a1) two-leg ladder model, (b1) three-leg ladder model and (c1) four-leg ladder model. (a2), (b2) and (c2). Energy spectrum for a finite chain with the width W . The horizontal axis is the site index. (a2) Nanoribbon described by Eq.(32) with the width $W = 2$, (b2) Nanoribbon with the width $W = 3$ and (c2) Nanoribbon with the width $W = 4$. Insets in (b2) show the enlarged energy spectrum in the vicinity of the zero energy, where red dots indicate the topological edge states, while cyan dots indicate the bulk states. Topological edge states emerge only for (b2). We have set $J = 0.5t$, $\mu = 0$ and $L = 20$. Color palette for (a) indicates $|\psi_1|^2 + |\psi_L|^2$, which is given in Fig.5(d).

L , each of which is composed of topological edge states. The effective Hamiltonian of one chain is given by

$$H_{\text{eff}} = t \sum_{y=1}^{W-1} \left(\hat{f}_y^\dagger \hat{f}_{y+1} + \hat{f}_{y+1}^\dagger \hat{f}_y \right), \quad (33)$$

for $W \geq 2$, where \hat{f}_y is an annihilation operator of the topological edge state. The energy spectrum is obtained as $E_{\text{eff}}(j) = t \cos(2\pi j/W + 1)$ with $j = 1, \dots, W$. There is one zero-energy state for odd W and no zero-energy state for even W . As a result, by considering two copies of the model and two edges, we have 4 zero-energy states for a nanoribbon with odd W .

A comment is in order. There are even-odd effects of the emergence of the edge or interface depending on the width of the ladder. It requires atomic scale layer control to observe the phenomenon in experiments.

V. MAJORANA FERMIONS

Majorana fermions are studied in the case of d -wave altermagnets[31–33]. We study Majorana fermions in p -wave magnets. We consider the case where s -wave superconducting pairing between up and down spins with opposite orbitals

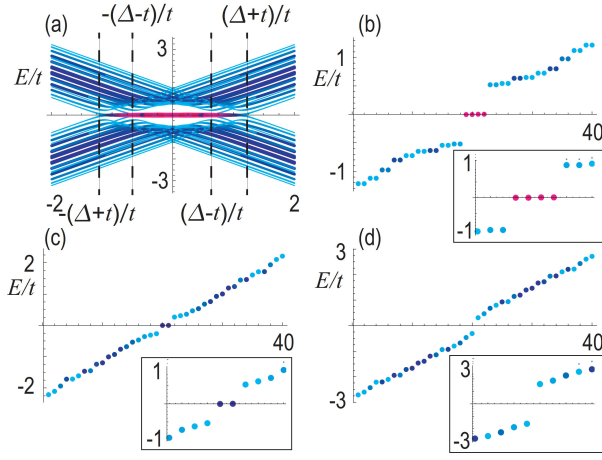


FIG. 7. (a) Energy spectrum as a function of μ/t . We have set $J = 0.5t$, $\xi = 1$ and $\Delta = 0.5t$. (b) Energy spectrum as a function of the state index with $\mu = 0$, where there are four zero-energy edge states. (c) $\mu = t$, where there are two zero-energy edge states. (d) $\mu = 2t$, where there are no zero-energy edge states. We have used a chain with the length $L = 10$. Color palette for (a) indicates $|\psi_1|^2 + |\psi_L|^2$, which is given in Fig.5(d).

is introduced via proximity coupling,

$$H_\Delta = \Delta \sum_{x,\tau=\pm 1} \left(c_{x,\uparrow,\tau} c_{x,\downarrow,-\tau} + c_{x,\downarrow,-\tau}^\dagger c_{x,\uparrow,\tau}^\dagger \right). \quad (34)$$

The Bogoliubov-de Gennes Hamiltonian is given by

$$\begin{aligned} H_{\text{BdG}} &= \begin{pmatrix} H_\uparrow(k) & \Delta \tau_x \\ \Delta \tau_x & -H_\downarrow(-k) \end{pmatrix} \\ &= [(t \cos k_x - \mu) \tau_z + J \tau_x \sin k_x] \otimes \zeta_z \\ &\quad + \Delta \tau_x \otimes \zeta_x. \end{aligned} \quad (35)$$

The energy spectrum is

$$E_{\text{BdG}} = \pm \sqrt{J^2 \sin^2 k_x + (t \cos k_x - \mu \pm \Delta)^2}. \quad (36)$$

The gap closes at $k_x = 0$ under the condition

$$t - \mu \pm \Delta = 0. \quad (37)$$

We show the energy spectrum as a function of μ in Fig.7(a). There are four Majorana zero-energy states for $|\mu| < t - \Delta$ as shown in Fig.7(b) and there are two Majorana zero-energy states for $t - \Delta < |\mu| < t + \Delta$ as shown in Fig.7(c). There is no zero-energy states for $|\mu| > t + \Delta$ as shown in Fig.7(d).

It is understood as follows. Actually, the Hamiltonian (35) is unitary equivalent to two copies of the Kitaev topological superconductor model,

$$U_{\text{BdG}} H_{\text{BdG}} U_{\text{BdG}}^{-1} = \begin{pmatrix} H_1 & 0 \\ 0 & H_2 \end{pmatrix} \quad (38)$$

with

$$H_1 = (t \cos k_x - \mu + \Delta) \sigma_z + J \sin k_x \sigma_x, \quad (39)$$

$$H_2 = (t \cos k_x - \mu - \Delta) \sigma_z + J \sin k_x \sigma_x, \quad (40)$$

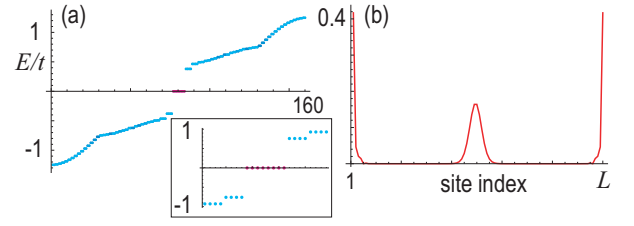


FIG. 8. (a) Energy spectrum with a p -wave magnetic domain wall. The inset shows an enlarged figure in the vicinity of the zero energy, where there are eight zero-energy states. They are four edge states and four interface states. (b) Spatial profile of Majorana Jackiw-Rebbi mode. We have used a chain with the length $L = 40$. We have set $J = 0.5t$, $\mu = 0$, $\xi = 5$ and $\Delta = 0.5t$. Color palette for (a) indicates $|\psi_1|^2 + |\psi_L|^2$, which is given in Fig.5(d).

where the unitary transformation is given by

$$U_{\text{BdG}} = \begin{pmatrix} 1 & 0 & 0 & 1 \\ 0 & -1 & 1 & 0 \\ 1 & 0 & 0 & -1 \\ 0 & 1 & 1 & 0 \end{pmatrix}, \quad (41)$$

where we have used the relations $U \Gamma_{zz} U^{-1} = \Gamma_{0z}$, $U \Gamma_{xz} U^{-1} = \Gamma_{0x}$ and $U \Gamma_{xx} U^{-1} = \Gamma_{zz}$.

The unit vector defined by

$$\mathbf{n}_j(k) \equiv H_j(k) / |H_j(k)| \quad (42)$$

points the z direction at $k = 0$ and π due to particle-hole symmetry. Then, we can define

$$n_j(k) \sigma_z = H_j(k) / |H_j(k)| \quad (43)$$

for $k = 0$ and π . As in the case of the Kitaev model, the topological index is the Z_2 index defined by

$$\nu \equiv n_j(0) n_j(\pi). \quad (44)$$

The system is trivial for $\nu = 1$, while the system is topological for $\nu = -1$. The Hamiltonian H_1 is topological for $|\mu| < t - \Delta$, while it is trivial for $|\mu| > t - \Delta$. On the other hand, the Hamiltonian H_2 is topological for $|\mu| < t + \Delta$, while it is trivial for $|\mu| > t + \Delta$. It well explains the result shown in Fig.7(d) because there emerge two Majorana edge states for each model in the topological phase.

The energy spectrum with the p -wave magnetic domain wall is shown in Fig.8(a). The spatial profile of the zero-energy states is shown in Fig.8(b), where the Majorana interface states are formed at the domain wall.

VI. DISCUSSIONS

We have investigated physical properties of p -wave magnets. The p -wave magnets are antiferromagnets just as altermagnets are. The Néel vector is observable by way of anomalous Hall effects in altermagnets. This is not the case in p -wave magnets. To overcome this, we have explored the

topological property. We have argued that the domain wall position will be detectable and controllable by electric field because it is a Jackiw-Rebbi state. Just as altermagnets have zero-net magnetization, p -wave magnets have zero-net magnetization.

Electron-electron interactions are neglected in the present study. There are several studies on interaction effects in the

SSH model[42–48]. The topological edge states are robust under the critical strength of electron-electron interactions, which is much smaller than that in ordinary materials. Then, it is adequate to neglect electron-electron interactions to study topological phases.

This work is supported by CREST, JST (Grants No. JP-MJCR20T2) and Grants-in-Aid for Scientific Research from MEXT KAKENHI (Grant No. 23H00171).

-
- [1] A. Yamaguchi, T. Ono, S. Nasu, K. Miyake, K. Mibu, and T. Shinjo, *Phys. Rev. Lett.* 92, 077205 (2004).
 - [2] Stuart S. P. Parkin Masamitsu Hayashi, Luc Thomas, Magnetic Domain-Wall Racetrack Memory, *Science* 320, 190 (2008).
 - [3] Gen Tatara and Hiroshi Kohno, Theory of Current-Driven Domain Wall Motion: Spin Transfer versus Momentum Transfer, *Phys. Rev. Lett.* 92, 086601 (2004).
 - [4] Gen Tatara, Hiroshi Kohno, Junya Shibata, Microscopic approach to current-driven domain wall dynamics, *Physics Reports* 468, 213 (2008).
 - [5] T. Jungwirth, X. Marti, P. Wadley and J. Wunderlich, Antiferromagnetic spintronics, *Nature Nanotechnology* 11, 231 (2016).
 - [6] V. Baltz, A. Manchon, M. Tsoi, T. Moriyama, T. Ono, and Y. Tserkovnyak Antiferromagnetic spintronics, *Rev. Mod. Phys.* 90, 015005 (2018).
 - [7] Jiahao Han, Ran Cheng, Luqiao Liu, Hideo Ohno and Shunsuke Fukami, Coherent antiferromagnetic spintronics *Nature Materials* 22, 684 (2023).
 - [8] Zhuoliang Ni, A. V. Haglund, H. Wang, B. Xu, C. Bernhard, D. G. Mandrus, X. Qian, E. J. Mele, C. L. Kane and Liang Wu, Imaging the Neel vector switching in the monolayer antiferromagnet MnPSe₃ with strain-controlled Ising order *Nature Nanotechnology* 16, 782 (2021).
 - [9] J. Godinho, H. Reichlov, D. Kriegner, V. Novak, K. Olejnik, Z. Kašpar, Z. Šoban, P. Wadley, R. P. Campion, R. M. Otxoa, P. E. Roy, J. Železný, T. Jungwirth and J. Wunderlich, Electrically induced and detected Neel vector reversal in a collinear antiferromagnet, *Nature Communications* volume 9, Article number: 4686 (2018).
 - [10] Kenta Kimura, Yutaro Otake and Tsuyoshi Kimura, Visualizing rotation and reversal of the Neel vector through antiferromagnetic trichroism, *Nature Communications*, 13, 697 (2022).
 - [11] Yi-Hui Zhang, Tsao-Chi Chuang, Danru Qu, and Ssu-Yen Huang, Detection and manipulation of the antiferromagnetic Neel vector in Cr₂O₃ *Phys. Rev. B* 105, 094442 (2022).
 - [12] L. Smejkal, A. H. MacDonald, J. Sinova, S. Nakatsuji and T. Jungwirth, Anomalous Hall antiferromagnets, *Nat. Rev. Mater.* 7, 482 (2022).
 - [13] L. Smejkal, J. Sinova, and T. Jungwirth, Beyond Conventional Ferromagnetism and Antiferromagnetism: A Phase with Non-relativistic Spin and Crystal Rotation Symmetry, *Phys. Rev. X*, 12, 031042 (2022).
 - [14] Libor Šmejkal, Jairo Sinova, and Tomas Jungwirth, Emerging Research Landscape of Altermagnetism, *Phys. Rev. X* 12, 040501 (2022).
 - [15] Amar Fakhredine, Raghottam M. Sattigeri, Giuseppe Cuono, and Carmine Autieri, Interplay between altermagnetism and nonsymmorphic symmetries generating large anomalous Hall conductivity by semi-Dirac points induced anticrossings, *Phys. Rev. B* 108, 115138 (2023).
 - [16] Teresa Tschirner, Philipp Keler, Ruben Dario Gonzalez Betancourt, Tommy Kotte, Dominik Kriegner, Bernd Buechner, Joseph Dufouleur, Martin Kamp, Vedran Jovic, Libor Smejkal, Jairo Sinova, Ralph Claessen, Tomas Jungwirth, Simon Moser, Helena Reichlova, Louis Veyrat, Saturation of the anomalous Hall effect at high magnetic fields in altermagnetic RuO₂, *APL Mater.* 11, 101103 (2023).
 - [17] Toshihiro Sato, Sonia Haddad, Ion Cosma Fulga, Fakher F. Assaad, Jeroen van den Brink, Altermagnetic anomalous Hall effect emerging from electronic correlations, *arXiv:2312.16290*
 - [18] Miina Leivisk Javier Rial, Anton Badura, Rafael Lopes Seeger, Ismaa Kounta, Sebastian Beckert, Dominik Kriegner, Isabelle Jomard, Eva Schmoranzarov Jairo Sinova, Olena Gomonay, Andy Thomas, Sebastian T. B. Goennenwein, Helena Reichlov Libor Smejkal, Lisa Michez, Tom Jungwirth, Vincent Baltz, Anisotropy of the anomalous Hall effect in the altermagnet candidate Mn₅Si₃ films, *Phys. Rev. B* 109, 224430 (2024)
 - [19] J. Krempask, L. Šmejkal, S. W. D'Souza, M. Hajlaoui, G. Springholz, K. Uhlov F. Alarab, P. C. Constantinou, V. Strocov, D. Usanov, W. R. Pudelko, R. Goncez-Hernandez, A. Birk Hellenes, Z. Jansa, H. Reichlov Z. Šob, R. D. Gonzalez Betancourt, P. Wadley, J. Sinova, D. Kriegner, J. Min, J. H. Dil and T. Jungwirth, Altermagnetic lifting of Kramers spin degeneracy, *Nature* 626, 517 (2024).
 - [20] Suyoung Lee, Sangjae Lee, Saegyeol Jung, Jiwon Jung, Donghan Kim, Yeonjae Lee, Byeongjun Seok, Jaeyoung Kim, Byeong Gyu Park, Libor Šmejkal, Chang-Jong Kang, Changyong Kim, Broken Kramers Degeneracy in Altermagnetic MnTe, *Phys. Rev. Lett.* 132, 036702 (2024).
 - [21] O. Fedchenko, J. Minar, A. Akashdeep, S.W. D'Souza, D. Vasilyev, O. Tkach, L. Odenbreit, Q.L. Nguyen, D. Kutnyakhov, N. Wind, L. Wenthau, M. Scholz, K. Rossnagel, M. Hoesch, M. Aeschlimann, B. Stadtmueller, M. Klauui, G. Schoenhense, G. Jakob, T. Jungwirth, L. Smejkal, J. Sinova, H. J. Elmers, Observation of time-reversal symmetry breaking in the band structure of altermagnetic RuO₂, *Science Advances* 10,5 (2024) DOI: 10.1126/sciadv.adj4883.
 - [22] T. Osumi, S. Souma, T. Aoyama, K. Yamauchi, A. Honma, K. Nakayama, T. Takahashi, K. Ohgushi, and T. Sato, Observation of a giant band splitting in altermagnetic MnTe, *Phys. Rev. B* 109, 115102 (2024)
 - [23] Zihan Lin, Dong Chen, Wenlong Lu, Xin Liang, Shiyu Feng, Kohei Yamagami, Jacek Osiecki, Mats Leandersson, Balasubramanian Thiagarajan, Junwei Liu, Claudia Felser, Junzhang Ma, Observation of Giant Spin Splitting and d-wave Spin Texture in Room Temperature Altermagnet RuO₂, *arXiv:2402.04995*.
 - [24] Makoto Naka, Satoru Hayami, Hiroaki Kusunose, Yuki Yanagi, Yukitoshi Motome and Hitoshi Seo, Spin current generation in organic antiferromagnets, *Nat. Com.* 10, 4305 (2019).
 - [25] Rafael Gonzalez-Hernandez, Libor Šmejkal, Karel Vbořn, Yuta Yahagi, Jairo Sinova, Tomš Jungwirth, and Jakub Železn. Effi-

- cient electrical spin splitter based on nonrelativistic collinear antiferromagnetism, *Phys. Rev. Lett.*, 126:127701, (2021).
- [26] M Naka, Y Motome, and H Seo, Perovskite as a spin current generator. *Phys. Rev. B*, 103, 125114, (2021).
- [27] Arnab Bose, Nathaniel J. Schreiber, Rakshit Jain, Ding-Fu Shao, Hari P. Nair, Jiaxin Sun, Xiyue S. Zhang, David A. Muller, Evgeny Y. Tsymlal, Darrell G. Schlom & Daniel C. Ralph, Tilted spin current generated by the collinear antiferromagnet ruthenium dioxide, *Nature Electronics* 5, 267 (2022).
- [28] K.-H. Ahn, A. Hariki, K.-W. Lee, and J. Kunes, Antiferromagnetism in RuO_2 as d-wave Pomeranchuk instability, *Phys. Rev. B* 99, 184432 (2019).
- [29] S. Hayami, Y. Yanagi, and H. Kusunose, Momentum-Dependent Spin Splitting by Collinear Antiferromagnetic Ordering, *J. Phys. Soc. Jpn.* 88, 123702 (2019).
- [30] Rafael M. Fernandes, Vanuildo S. de Carvalho, Turan Birol, Rodrigo G. Pereira, Topological transition from nodal to nodeless Zeeman splitting in altermagnets, *Phys. Rev. B* 109, 024404 (2024).
- [31] Di Zhu, Zheng-Yang Zhuang, Zhigang Wu, and Zhongbo Yan, Topological superconductivity in two-dimensional altermagnetic metals, *Phys. Rev. B* 108, 184505 (2023).
- [32] Yu-Xuan Li and Cheng-Cheng Liu, Majorana corner modes and tunable patterns in an altermagnet heterostructure, *Phys. Rev. B* 108, 205410 (2023).
- [33] Sayed Ali Akbar Ghorashi, Taylor L. Hughes, Jennifer Cano, Altermagnetic Routes to Majorana Modes in Zero Net Magnetization, arXiv:2306.09413
- [34] M. Ezawa, Detecting the Neel vector of altermagnet by attaching a topological insulator and crystalline valley-edge insulator *Phys. Rev. B* 109, 245306 (2024)
- [35] Yu-Xuan Li, Yichen Liu, and Cheng-Cheng Li, Creation and Manipulation of Higher-Order Topological States by Altermagnets, *Phys. Rev. B* 109, L201109 (2024)
- [36] Anna Birk Hellenes, Tomas Jungwirth, Jairo Sinova, Libor Šmejkal, Unconventional p-wave magnets, arXiv:2309.01607.
- [37] Kazuki Maeda, Bo Lu, Keiji Yada, Yukio Tanaka, Theory of tunneling spectroscopy in p-wave altermagnet-superconductor hybrid structures, arXiv:2403.17482.
- [38] B. Andrei Bernevig, Taylor L. Hughes, Shou-Cheng Zhang, Quantum Spin Hall Effect and Topological Phase Transition in HgTe Quantum Wells, *Science*, 314, 1757 (2006).
- [39] Shinsei Ryu, Andreas Schnyder, Akira Furusaki, Andreas Ludwig, Topological insulators and superconductors: ten-fold way and dimensional hierarchy, *New J. Phys.* 12, 065010 (2010)
- [40] R. Jackiw and C. Rebbi *Phys. Rev. D* 13 3398 (1976).
- [41] Ryohei Wakatsuki, Motohiko Ezawa, Naoto Nagaosa, Domain wall of a ferromagnet on a three-dimensional topological insulator, *Scientific Reports* 5, 13638 (2015).
- [42] W. Chen, Weakly interacting topological insulators: Quantum criticality and the renormalization group approach, *Physical Review B* 97, 115130 (2018).
- [43] J. Sirker, M. Maiti, N. P. Konstantinidis, and N. Sedlmayr, Boundary fidelity and entanglement in the symmetry protected topological phase of the SSH model, *Journal of Statistical Mechanics: Theory and Experiment* 2014, P10032 (2014).
- [44] A. M. Marques and R. G. Dias, Multihole edge states in Su-Schrieffer-Heeger chains with interactions, *Physical Review B* 95, 115443 (2017).
- [45] M. Yahyavi, L. Saleem, and B. Hetenyi, Variational study of the interacting, spinless Su-Schrieffer-Heeger model, *Journal of Physics: Condensed Matter* 30, 445602 (2018).
- [46] T. Jin, P. Ruggiero, and T. Giamarchi, Bosonization of the interacting Su-Schrieffer-Heeger model, *Physical Review B* 107, L201111 (2023).
- [47] P. B. Melo, S. A. S. Jior, W. Chen, R. Mondaini, and T. Paiva, Topological marker approach to an interacting Su-Schrieffer-Heeger model, *Physical Review B* 108, 195151 (2023).
- [48] E. Di Salvo, A. Moustaj, C. Xu, L. Fritz, A. K. Mitchell, C. Morais Smith and D. Schurichtm, Topological phases of the interacting SSH model: an analytical study, arXiv:2408.01421